LANGMUIR

pubs.acs.org/Langmuir Article

Understanding Coal Fly Ash Glass Depolymerization and Colloidal Silica Formation toward Controlled Rare Earth Extraction

Yihan Li and Wen Song*

Cite This: *Langmuir* 2026, 42, 23461−23470 Read Online

ABSTRACT: In recent years, coal fly ash (CFA) has emerged as a sustainable alternative resource for rare-earth elements (REEs). Acid leaching enables efficient REE recovery, yet large-scale processing is hindered by the formation of silica gels that immobilize REE-bearing leachates. This work investigates the depolymerization of the amorphous aluminosilicate glass phase in CFA and its role in the generation of colloidal silica during acid leaching. Structural and chemical analyses reveal that under highly acidic conditions (pH < 1), proton-mediated rupture of metal−oxygen bonds releases short-chain silica species (e.g., dimers and trimers) from the glass network without complete dissolution of Si-rich particles. The mobilized short-chain silica then undergoes hydrolysis and condensation in the leachate solution to form polymerized siloxane networks (i.e., gels). The structural characterization and chemical speciation analyses presented here help elucidate the roles of ion concentration, pH, acid/ash ratio, and ash crystallinity in initiating gel growth and provide mechanistic insights for improving the feasibility of industrial-scale REE recovery processes to enable CFA as an abundant resource for REEs.

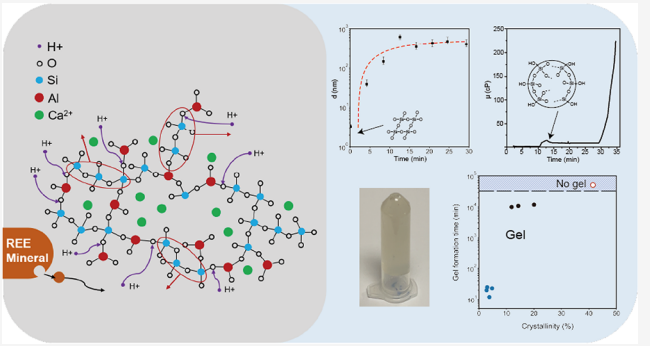

INTRODUCTION

Rare earth elements (REEs), including the lanthanides, yttrium, and scandium, are essential materials in advanced technologies due to their exceptional optical, electrical, and magnetic properties.[1−3] The global demand for REEs, particularly magnet elements such as neodymium, praseodymium, dysprosium, and terbium, has nearly doubled since 2015, surpassing 90 kt in 2024.[4] Conventional large-scale open-pit mining and hydrometallurgical extraction methods are usually associated with significant water consumption and waste emissions.[5−7] Therefore, researchers have increasingly focused on developing economically feasible, environmentally friendly, and domestically sustainable alternatives for REEs. Coal fly ash (CFA), a byproduct of coal combustion, contains an average REE concentration of up to ∼445 ppm globally.[8−11] According to the American Coal Ash Association, approximately 32 million short tons of coal fly ash are produced annually, yet only about 60% is reused, mainly in building materials, zeolite synthesis, concrete, and agriculture.[12−14] The remaining fly ash is typically disposed of in unlined landfills, where heavy metals such as mercury, cadmium, arsenic, and lead cause long-term contamination if leaked into surface water or groundwater.[15,16] Repurposing CFA as a secondary source for REEs therefore offers a dual benefit of remediating the impact of industrial waste contamination and reducing the environmental footprint of conventional REE mining.

In coal fly ash, approximately 78% of REEs are bound within its dense (i.e., nonporous) amorphous aluminosilicate glass phase, where REE recovery is governed by the intermolecular diffusion of glassy matrices enabled by alkali and alkali-earth metals without bulk dissolution.[17,18] Specifically, major metals such as Al, Ca, and Fe are extracted layer by layer from the particle matrix during leaching as they diffuse outward through the vacated molecular interstices in exchange for protons from the leachant.[17,19] Previous studies have shown that using nitric acid as the leaching reagent at room temperature, acid leaching-induced solid-state interdiffusion has increased the total REE recovery rate to ∼70% without the need for complete digestion of the ash matrix.[11,17,20] However, field-scale application of acid leaching is hindered by the formation of gelatinous phases even under highly acidic conditions (pH < 1), particularly in samples with high Ca content and low crystallinity.[18,19,21] Particularly, these gels form homogeneously throughout the leachate and viscosify the REE-bearing solution.[22−24] Current approaches to separate REEs from the leachate include solvent extraction, coprecipitation, membrane separation, adsorption, and ion exchange, all of which require fluid handling.[25−29] Gel formation immobilizes the REE-bearing leachate, fundamentally impedes

Received: April 27, 2026
Revised: July 28, 2026
Accepted: July 29, 2026
Published: August 6, 2026

https://doi.org/10.1021/acs.langmuir.6c02451
Langmuir 2026, 42, 23461−23470

sequential separation methods, and limits large-scale and industrial application.[24,30] Therefore, understanding the mechanisms of gel formation is critical to prevent leachate gelation and enable practical liquid-based REE extraction methods.

Existing research on CFA-related gels has focused primarily on those formed under alkaline and aqueous environments, typically induced by H_2O, NaOH, or $Ca(OH)_2$. In alkaline systems, Ca acts as a network modifier, strengthening the structure of calcium−aluminosilicate−hydrate (CASH) or sodium−aluminosilicate−hydrate (NASH) gels.[30−33] In aqueous conditions, the corrosion process was explained by 2 models: the dissolution/reprecipitation model posits that the glass dissolves congruently within a thin film of interfacial water and that the gel forms by precipitation of sparingly soluble species, generating a passivating gel layer that envelops the glass in a core−shell configuration and reduces subsequent reaction rates;[34−39] and the continuous gel reorganization model suggests that water molecules diffuse through the open gel porosity and react with (Si, Al, and Zr)−O−Si bonds, dynamically opening and closing pores within the gel, which exerts a passivating effect.[35,40] However, gel structures and formation mechanisms under acidic conditions have not been systematically explored. Since metal ions like Al and Ca exhibit higher solubility under acidic conditions, the gel formed during acid leaching may differ in structure, morphology, as well as its influence on reaction kinetics and diffusion.

This work investigates the conditions and mechanisms that promote gelation during the acid leaching of coal fly ash and delineates the origin of the gel constituents. Structural characterization and chemical speciation analyses are performed to probe the roles of ion concentration, pH, acid/ash ratio, and ash crystallinity in initiating gel growth under acidic conditions and to elucidate the mechanisms of bond disruption and phase evolution that drive the release and transformation of silica species to form colloidal gels. The main contributions of this work are threefold. First, in contrast to previous studies on gel formation and glass corrosion under alkaline or aqueous conditions, this work focuses on the highly acidic glass depolymerization and gel formation mechanisms of direct relevance to the hydrometallurgical processing of industrial materials. Second, this work presents a gel formation phase diagram under highly acidic environments that serves as a practical reference framework for industrial-scale REE recovery. Third, the findings presented here highlight coal fly ash as a reactive aluminosilicate glass platform capable of generating functional silica colloids through controlled depolymerization.

MATERIALS AND METHODS

Materials

Four different coal fly ash samples were used in this work. The elemental composition of each ash sample was characterized by full acid digestion. Total REE concentrations range from 338 to 622 ppm, with silicon and aluminum concentrations (presented in the form of oxides) typically ∼20 wt % and iron concentrations (presented in the form of oxides) ∼5 wt %. According to the American Society for Testing and Materials (ASTM) standard C618,[41] FA-6 is Class C coal fly ash with a higher calcium concentration (∼32 wt % in the form of oxides) and is typically produced from burning lignite or subbituminous coal. FA-1, FA-5, and FA-7 are Class F coal fly ash with calcium concentrations (presented in the form of oxides) < 18 wt % and are typically derived from burning anthracite or bituminous coal. Additionally, FA-1 is also iron-rich fly ash (iron concentration ∼ 21%, in the form of oxides, Fe_2O_3). A summary of the basic information on all samples mentioned is listed in Table S1.

XRD patterns and SEMs of the CFA samples are shown in Figure S1. CFA particles are mostly spherical, with particle sizes ranging from ∼0.1 to 100 μm. Amorphous aluminosilicate glass is the main mineral phase in all four samples, and quartz and mullite are the main crystalline phases. FA-6 shows a more complex composition, with the presence of anhydrite and lime in the structure, consistent with the high Ca concentration revealed by elemental analysis. Hematite is detected in FA-1, which also explains why FA-1 exhibits a darker color and a stronger magnetic response.

Acid Leaching Experiment

Acid leaching experiments were conducted using nitric acid with concentrations ranging from 1 to 15 M and acid-to-ash ratios from 1 to 50 (m/m). The resulting solid and liquid phases were analyzed separately to understand the cation exchange during the leaching process and the secondary phase precipitation formation mechanism. After acid leaching, the leachate was transferred to a clean centrifuge tube and centrifuged for 5 min at 10,000 rpm to separate the liquid and solid phases.

The solid precipitation was washed with water three times and with acetone once and then thoroughly dried at 100 °C for microscopy analysis of microstructural features and spatial ion distribution at cross-sections. The liquid phase was centrifuged again at 10,000 rpm for 5 min to remove possible condensation and diluted for ICP-MS analysis. The gel phase was soaked in deionized water for 48 h to remove residual leachate species (e.g., Al, Ca, Fe) entrapped within the gel framework. Subsequent washing and ultrasonication were repeated several times, and the clean gel product was collected.

Materials Characterization

The phases present in the coal fly ash samples—both crystalline and amorphous—was characterized using X-ray diffraction (XRD, Rigaku Miniflex 600 Diffractometer II). Ash crystallinity was calculated by accounting for the amorphous content using Jade (% crystallinity = $V_{\text{crystalline phase}}/V_{\text{total}}$). Microscale fly ash morphology and elemental distributions were mapped using scanning electron microscopy (SEM, Apreo 2C LoVac) and energy-dispersive X-ray spectroscopy (EDS, Bruker).

The composition and bonding structure of the secondary precipitates were elucidated using Fourier transform infrared spectroscopy (FTIR, Bruker Invenio R). Cation concentrations of the leachate were collected using ICP-MS (Agilent 8900 Triple Quadrupole) to understand the effect of different metal ions on gel formation. To prepare samples for time-resolved ICP-MS, leaching solution samples were collected under controlled temperature (20 °C) at defined time intervals (0, 1, 2, 3, 4, 5, 6, 10, 20, and 30 min) throughout the reaction and then immediately centrifuged to separate the liquid and solid phases. The liquid phase was subsequently diluted 5000 times to ensure that analyte concentrations fell within typical calibration ranges. The experiments were performed in triplicates, and additional results are listed in Figures S3 and S4.

To understand the origin of the gel-forming species, microscale spatiochemical characterization was performed on the reacted fly ash particles. Specifically, the reacted ash was mounted in epoxy and polished to reveal internal cross-sections for SEM-EDS. Lamellae were extracted from the reacted particles using focused ion beam (FIB-SEM) and imaged using transmission electron microscopy (TEM) paired with electron energy loss spectroscopy (EELS) for coordination analyses.

Over the course of ash/acid reactions, the dissolved silica particle size change was measured by Dynamic Light Scattering (DLS) to elucidate gelation mechanisms. To perform a time-resolved DLS measurement, a baseline control was first established by measuring an HNO_3 solution without coal fly ash as a blank to confirm the absence of dust or background scatter. Then, under controlled temperature (25 ± 1 °C), measurements were taken at defined intervals to capture a smooth growth curve, with the PDI maintained at <0.3 to ensure that the observed signal reflected particle growth instead of agglomeration. Additionally, cross-validation with complementary techniques was performed by measuring the continuous change in the viscosity of the leachate. Specifically, leaching reactions were initiated in a syringe loaded with ash by drawing in 6 M HNO_3. The leachate was then

https://doi.org/10.1021/acs.langmuir.6c02451
Langmuir 2026, 42, 23461−23470

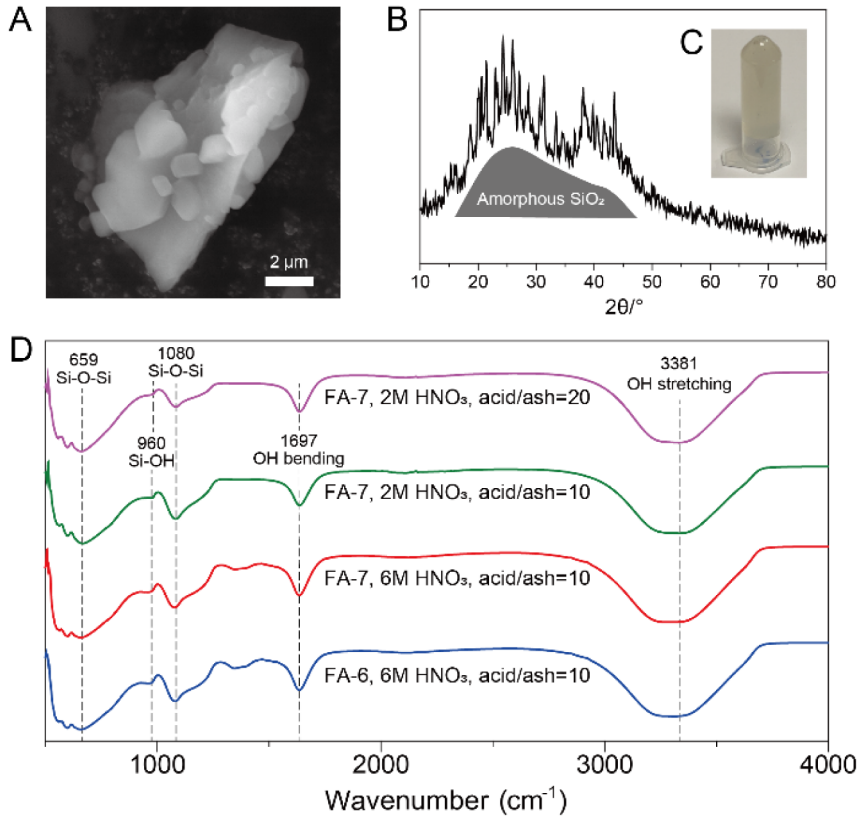

Figure 1. Physicochemical characteristics of the gelled acid leachate during REE extraction from fly ash. (A) Morphology characterization of the wet gel by SEM shows a dense and aggregated gel framework. (B) XRD of the dehydrated gel shows a broad peak between 20° and 25° that indicates an amorphous SiO_2 structure. (C) A translucent semisolid phase formed throughout the acidic leachate over the course of REE extraction. The gel is rigid and immobile. (D) FTIR results of the washed gel in its original hydrated condition. Characteristic transmittance peaks were observed at 1080 cm^{-1} (Si−O−Si bond stretching), 960 cm^{-1} (Si−OH), and 3381 cm^{-1} (O−H stretching).

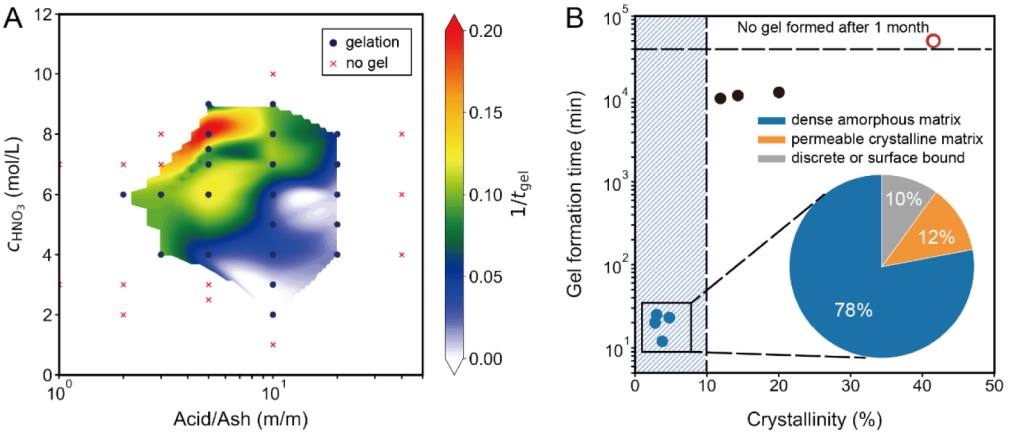

Figure 2. (A) Phase diagram mapping the gelation behavior of coal fly ash sample FA-7 under different nitric acid concentrations and acid/ash mass ratios. The colored region indicates conditions under which gel formation occurs. When the acid concentration is below 2 M or above 9 M, gelation is largely suppressed. (B) The crystallinity of the original coal fly ash sample strongly influences the gel formation tendency. Amorphous ashes (i.e., crystallinity < ∼10%) form gels readily, whereas for ashes with crystallinity exceeding 40%, there is no sign of gel formation after a month of leaching.

filtered and injected at a constant flow rate (q = 0.1 mL/min) into smooth PTFE tubing (L = 50 cm, r = 125 μm) to measure its viscosity over time according to the Hagen−Poiseuille equation:

$$\mu = \frac{\pi r^4}{8qL}\Delta P$$

where the pressure drop, ΔP, is the difference between pressure sensor measurements at the inlet of the tubing and the pressure at the tubing outlet, which was maintained at atmospheric conditions.

RESULTS AND DISCUSSION

Gel Formation

During acid leaching of REEs from CFA, the leachate transits into a translucent semisolid gel (Figure 1C). The SEM result (Figure 1A) shows a cluster of irregular structures, with a broad size distribution from 1 to 10 μm. While the gelled leachates are amenable to ion diffusion, gel formation limits their fluidity and, hence, their ability to be transported during commercial

https://doi.org/10.1021/acs.langmuir.6c02451
Langmuir 2026, 42, 23461−23470

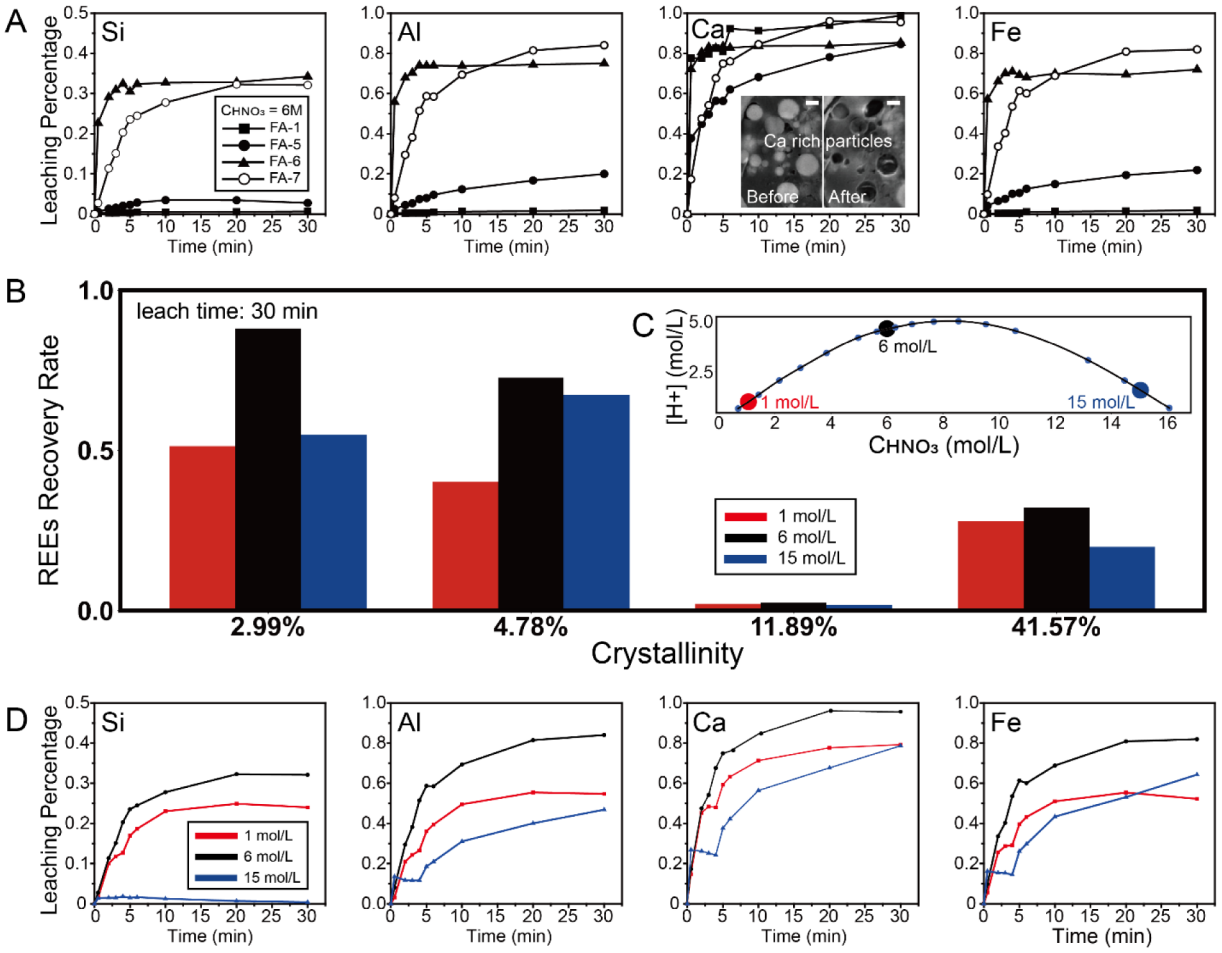

Figure 3. Dissolution behavior of (A) Si, Al, Ca, and Fe in different coal fly ash samples. (D) The extraction rate of Si, Al, Ca, and Fe from FA-7 ash under different nitric acid concentrations. ICP-MS results indicate that leaching reactions occur rapidly, with most reactions completing within the first 6 min and cation concentrations stabilizing after approximately 10 min. After 30 min, ~90% of Ca is leached from the ash structure. (B) Total REE recovery rates from ash samples with different crystallinities under 1, 6, and 15 mol/L nitric acid leaching. (C) The dissociation equilibrium of HNO_3 suggests that the number of free protons (H^+) available in solution increases less efficiently at higher acid concentrations.[42]

processing. Such behavior is fundamentally unfavorable for industrial REE recovery and motivates the need to understand the conditions and mechanisms that promote gelation, as well as the origin of its constituents.

Compositional and molecular analyses using FTIR show that the gel framework is constructed primarily of Si−O bonds with Si−OH groups on the surface (Figure 1D, Figure S5). The hydrated gel retains water within its cross-linked network and does not dissolve when dispersed in water or even in HNO_3. Altogether, the physical characteristics of the secondary gel precipitate are consistent with those of a hydrogel. XRD characterization of the heat-dried gel (100 °C for 3 h to remove internal water) further confirms an amorphous SiO_2 structure. While gel onset times vary for the different ash samples tested, the original chemical composition of CFA (Figure S1), acid concentration, and acid/ash ratio have little influence on the composition and properties of the resulting gel (Figure 1D). For example, gels formed under the same acid concentration and acid/ash ratios for FA-6 (32% Ca, 17% Al, 15% Si) and FA-7 (12% Ca, 19% Al, 26% Si) as well as gels formed under different acid concentrations (2 M and 6 M) for FA-7, hold identical molecular structures.

Despite possible chemical reactions between the acid and secondary cations (e.g., Ca and Al), surprisingly, the released Al and Ca ions do not participate in the gel construction. This distinguishes these acid-derived gels from typical Al- and Ca-rich gels formed under alkaline conditions.[31,32]

Gel Formation Conditions

While the gels produced from the acid leaching of different REE-bearing ashes are identical in structure, the rate of their formation differs (Figure 2). The set of conditions that result in leachate gelation was mapped to understand the origin of the gel and the conditions that lead to their cross-linking (Figure 2). Phase diagrams comparing leachant acidity (i.e., $cHNO_3$) and leachant-to-solid (i.e., acid/ash) ratios are drawn for the FA-7 ash sample to delineate the compositional and chemical controls on gelation (Figure 2A). Specifically, lower leachant acidity (e.g., 1 M HNO_3) successfully avoids gel precipitation as a result of insufficient leaching stoichiometry, but is encumbered by poor REE extraction. Increasing the acid concentration to ranges amenable to economic REE extraction, however, results in rapid gel condensation (~10−30 min). While further acidity does not necessarily promote gel formation (e.g., acid concentrations exceeding 9 M suppressed gelation), the highly acidic leachant becomes economically prohibitive for REE extraction and is unfavorable.

Similarly, acid/ash ratios (m/m) influence gelation non-linearly. At high acid/ash ratios, the dissolved reaction products

https://doi.org/10.1021/acs.langmuir.6c02451
Langmuir 2026, 42, 23461−23470

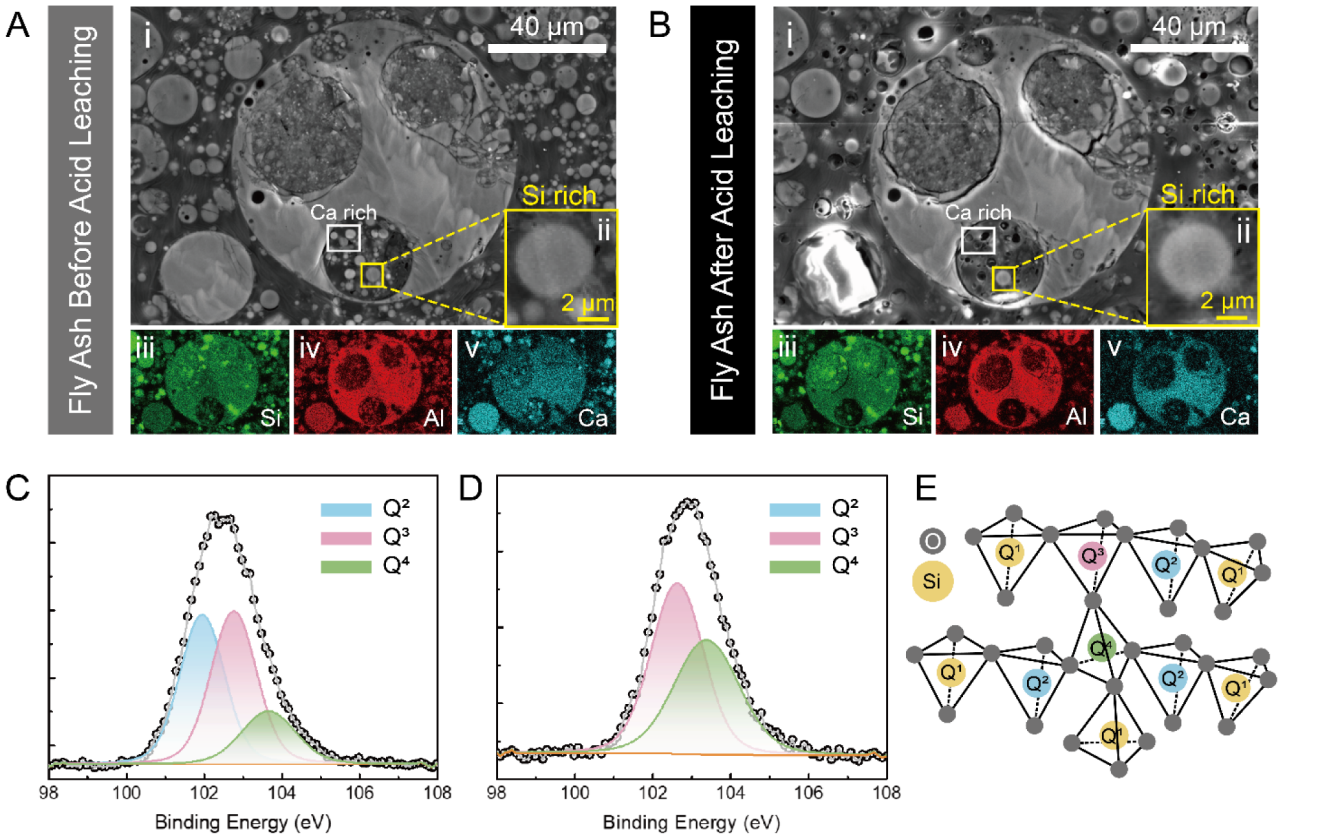

Figure 4. SEM-EDS results of A (i)−(v) original coal fly ash particles of FA-7 and B (i)−(v) particles after acid leaching show that Ca-rich particles are almost completely reacted with the acid, leading to the collapse of the entire particle structure, while Si-rich particles are only partially dissolved, resulting in particle shrinkage. XPS spectra of Si 2p from (C) original coal fly ash particles and (D) leached particles indicate the presence of Q structures of SiO_4. Q^2 structures dominate in raw CFA but disappear after acid leaching. Silica dimers are leached entirely, while larger (e.g., tetramers) remain. (E) Position of Q^n Si tetrahedra in a finite silica chain.

are too dilute for the gels to condense. We note that, while gels do not form here, the extracted REEs are likewise diluted in the leachate and result in limited downstream REE separability. For acid/ash ratios of less than 1:5, the leachate forms a highly viscous slurry (i.e., cement) that binds the extracted REEs into a secondary solid mass. Overall, the range of acidities and acid/ash ratios feasible for economic REE recovery coincides with rapid gelation and requires an understanding of the origins of the gel-forming species.

Interestingly, XRD characterizations show that gel formation is also fundamentally controlled by the crystallinity of the ash matrix (Figure 2B). Under the same leaching conditions, reactions with fly ash samples comprised primarily of an amorphous glass (i.e., aluminosilicate glass with crystallinity < ~10%) generally formed gel much more rapidly compared to those with high crystallinity. Specifically, 2 M HNO_3 leachates of highly amorphous ashes (i.e., FA-3, FA-4, FA-6, and FA-7, crystallinity < ~5%) transitioned to complete gel in ~30 min. Gel onset times for crystalline ashes (i.e., crystallinity >10%, samples FA-1, FA-2, FA-8), on the other hand, exceeded a week. Ashes with even less amorphicity (e.g., FA-5 with crystallinity exceeding 40%) showed no sign of gel formation even after a month, suggesting that gelation is unlikely to occur. This suggests that the presence of more amorphous glasses in the ash promotes the formation of gels due to their high reactivity and solid-state diffusivity, whereas crystalline phases—mainly quartz and mullite—do not contribute to gel formation.

Acid Leaching and Gel Formation Mechanism

As inferred from the XRD and crystallinity results, reactions occurring within the amorphous phase are the primary cause of gel formation. Yet, the leachate HNO_3 fails to break the Si−O bonds of the amorphous glass, obfuscating the source of the Si−O.

To understand the origin of the gel-forming Si−O, we first examine the leachate composition over time (Figure 3). Time-resolved ICP-MS of leachates reacting with FA-7 shows that leaching proceeds rapidly for amorphous ashes, with most reactions completed within the first 6 min and cation concentrations stabilizing after ~10 min (Figure 3A, Figure S2). Comparison across fly ash samples (Figure 3A) shows that increased crystallinity (e.g., FA-1, FA-5) is correlated with lower extracted cation concentrations in the leachate, possibly as a result of diminished solid-state reactivity and diffusivity.

The high Ca recovery percentage compared to Al and Si, especially in crystalline samples (Figure 3A, FA-5), suggests a different chemical environment for Ca. While the stronger electronegativity difference of Ca−O bonds results in faster Ca extraction, their near-complete recovery (i.e., recovery ~ 1, Figure 3A) suggests causes beyond reaction kinetics alone. For example, even in crystalline FA-5, more than 80% of Ca is leached after 30 min and suggests that Ca in the ash structure is present as weakly held charge-compensating ions within the aluminosilicate glass matrix rather than covalently bonded with Al−O or Si−O structures. While the concentration of Ca does not directly affect the kinetics of metal-oxide bond breakage, the

https://doi.org/10.1021/acs.langmuir.6c02451
Langmuir 2026, 42, 23461−23470

removal of Ca creates molecular interstices for H+ diffusion that can increase the overall rate of the reaction in Ca-abundant samples. As shown in Figure 3, FA-6 and FA-7 exhibit comparable crystallinity and recovery rates for the major ions (Al, Fe, Ca) and REEs, but at the same acid concentration and acid/ash ratio, FA-6 (~32 wt % Ca in the form of oxides) exhibits a notably higher overall reaction rate (Figure 3A).

The leachate concentration changes under different acidities highlight the influence of free proton availability on ion extraction and gelation (Figure 3B–D). At low acid concentrations (i.e., $cHNO_3 < 2$ M), SiO_2 are released from the ash but are diluted and unable to polymerize into extended gel frameworks (i.e., insufficient chain formation). At high acid concentrations, water becomes relatively scarce, and the limited availability of water–water hydrogen bonding promotes the formation of additional hydrogen bonds between water molecules and HNO_3(aq) (Figure 3C).[42−44]

Comparison of 6 M HNO_3 leaching of CFA samples shows that REE recovery rates vary inversely with crystallinity (Figures 2B and 3B). In glassy ash particles, crystal grains are interspersed, where covalently bonded cations in the crystal lattice fail to hydrolyze and generate the intraparticle pathways. As a result, access for H+ to REE-bearing minerals that are surrounded by crystalline phases is limited by the availability of intercrystalline pores, resulting in lower recovery rates. For the same CFA sample, comparing the leaching results at different acid concentrations reveals that higher proton availability in the solution increases REE recovery. Consistent with the dissociation equilibrium of HNO_3 (Figure 3C), where $[H+]_{6M} > [H+]_{15M} \approx [H+]_{1M}$, leaching with 6 M HNO_3 produces the highest REE recovery for all 4 samples. In particular, 6 M HNO_3 leaching recovered ~88% total REEs from FA-7, with final REE concentrations of ~31 ppm in the solution. Extremely low REE recovery rates from FA-1 are a result of its relatively high crystallinity and Fe content. Additional data regarding REE recovery rates under different acid concentrations and acid/ash ratios are included in Table S2.

While solution analyses establish that acid leaching of the CFA contributes to silica dissolution into the leachate, SEM imaging shows that the Si-rich particles exhibit no structural collapse (Figure 4A,B) compared to Ca-rich particles, which fully disappeared over the course of leaching. Therefore, HNO_3 leaching here does not digest the bulk CFA silica structure to extract the resident REEs. Previous studies showed that complete digestion of the bulk CFA matrix is not necessary for effective REE extraction; in fact, bulk digestion using HF leads to the formation of recalcitrant $REEF_3$ precipitates, consumes uneconomic quantities of reagents, and introduces additional impurity cations to the leachate that are difficult to separate. HNO_3 leaching, on the other hand, encourages proton-metal exchange and interdiffusion in the solid amorphous matrix to enable REE extraction without disrupting the bulk silica framework.

To understand the source of the gel-forming Si–O in solution, XPS analyses were performed on the ash particles to determine their silica tetrahedron coordination (i.e., Q^n structure) before and after leaching (Figure 4). Here, Q^n denotes the number of bridging oxygen atoms in SiO_4 units, with n = 1 to 4 (Figure 4E).[45,46] For example, a Q^1 silica tetrahedron shares only 1 oxygen atom with an adjacent silica, implying that the other three oxygens are bonded with other species such as Ca or Al. In the original CFA, Q^2 and Q^3 structures dominate (Figure 4C). Reaction with HNO_3 consumes the reactive Q^2 structures entirely, along with some Q^3 structures; the residual silica in the ash is comprised of the remaining (i.e., unreacted) Q^3 and Q^4 structures (Figure 4D, Table 1). In other words, HNO_3 leaching breaks enough oxygen bonds with Ca/Al so that the attached silica dimers and trimers (i.e., Q^2 and Q^3 structures) are released from the unreactive Q^4 silica mainframe and diffuse out of their molecular interstices. Given that the Si-rich particles remain intact over the course of leaching (Figure 4A,B), the mobilization of short-chain silica (i.e., Q^2 and Q^3) provides a plausible explanation for the source of the gel-forming silica.

Table 1. Q Structures of FA-7 Solid Residue before and after Acid Leaching

		Percentage (%)	
Q^n	Binding Energy (eV)	Original CFA	After acid leaching
Q^2	101.5	40.37	0
Q^3	102.5	42.28	54.5
Q^4	103.5	17.36	45.5

We note here that unlike the passive layers formed during conventional glass corrosion, no growth of a passivating shell encapsulating the particle was observed. Instead, gel forms throughout the leaching solution, and separating the solid residues from the leachate did not inhibit gel formation. Meanwhile, for ash samples with low crystallinity, the gel formed here does not hinder the reaction itself, and the leaching percentage of the major cations (Al, Ca, and Fe), as well as the REE recovery rate, exceeds 80%. The major impact of gel formation is instead the loss of bulk fluidity: large volumes of liquid and dissolved ions become trapped within the gel framework, thereby impeding subsequent REE separation processes.

Core–Shell Structure in High-Crystallinity CFA and Local Si Diffusion Limit

During acid leaching of the high-crystallinity sample (i.e., FA-5 with crystallinity of ~40%), the Si leaching percentage remains low (<20%) even when the reaction reaches equilibrium and the concentrations of major cations (Al, Ca, and Fe) have stabilized (Figure 3A). Here, gelation is suppressed due to the low reactivity of crystalline phases (e.g., quartz, mullite), which results in insufficient silica particles being released into the solution during leaching and inadequate generation of interstitial pathways for protons to access the REE-bearing minerals within the particles. Ultimately, suppressed silica release in glassy ashes leads to reduced REE recovery rates (Figure 3B).

Cross-sectional observation of the leached FA-5 particles reveals a core–shell structure (Figure 5A). SEM–EDS analyses show a radially dependent cation distribution: for major cations (i.e., Al, Ca, Fe), concentrations gradually decrease along the radius within the core and are nearly absent in the shell. Si, however, exhibits an inverse trend: Si concentrations increase slightly within the core, reach a maximum at the core–shell boundary, and then decrease sharply in the shell. We note, however, that the so-called shell is a remnant of the original ash particle and not a redeposition of dissolved silica as described by the standard dissolution-reprecipitation model since Si-rich particles do not show a significant change in particle size or shape before and after the reaction (Figure 4).

TEM characterization reveals distinct chemical environments in the core and shell regions (Figure 5B i, ii). The Si $L_{2,3}$-edge

https://doi.org/10.1021/acs.langmuir.6c02451
Langmuir 2026, 42, 23461−23470

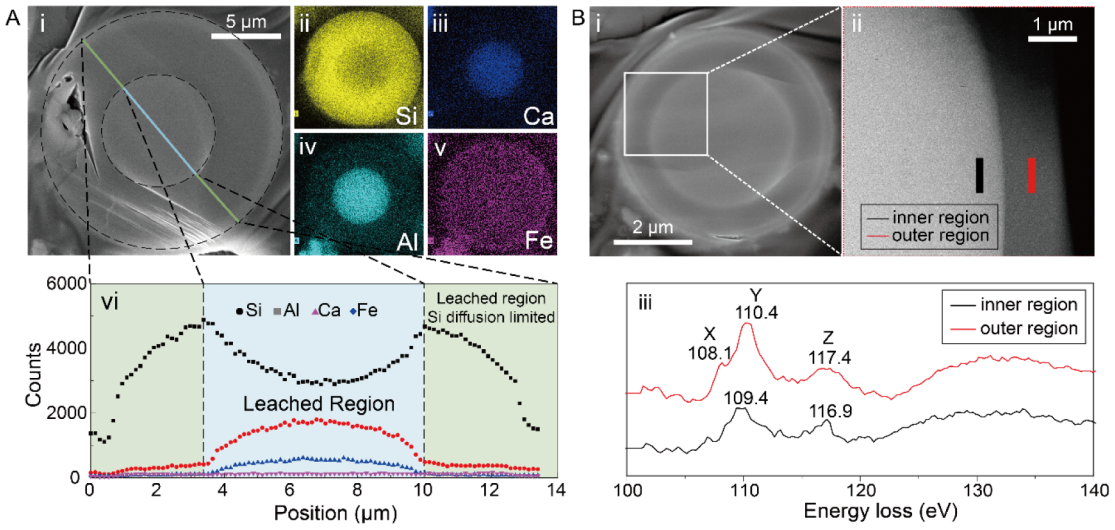

Figure 5. SEM (A) and TEM (B) of cross section show the concentration gradient and chemical environment changes in the core−shell structure of acid-leached FA-5 particles. Concentration decreases from core to shell for Al, Ca, and Fe, while for Si, the concentration increases in the core and then decreases along the radius in the shell.

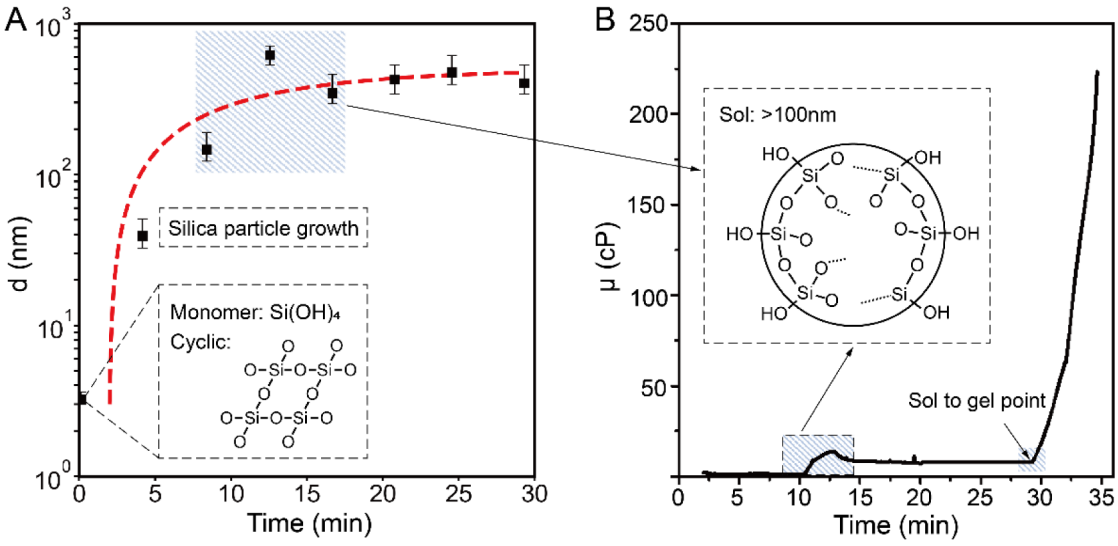

Figure 6. (A) DLS measurements show that the dissolved silica sizes increase over time during acid leaching. The particle growth can be fitted with an exponential curve, consistent with the Arrhenius activation energy equation. At ∼10 min, dissolved SiO_2 reached sol dimensions (>100 nm). Each data point represents the mean of three independent experiments, with error bars indicating the deviation. (B) Viscosity of the liquid phase increases at 10 min first when the sols begin forming and then again at 30 min when the solution condenses into a gel.

fine structure shows a main peak at 109−110 eV, characteristic of Si^{4+}. The presence of bridging bonds (Q^n structures) and the introduction of other metals influence the polarization of Si−O bonds, resulting in a chemical shift in EELS peaks. During the transition of the Si structure from Q^4 to Q^2, the main peak (Figure 5B iii, peak Y) shifts to a lower energy, while the presence of metals leads to broadening and asymmetry of peak Y and broadening of peak Z (Figure 5B (iii)). Increased local coordination disorder suppresses band splitting, weakens the separation between L_2 and L_3, and reduces the extended fine structure.[46,47] Consequently, Si in the shell exhibits a chemical environment dominated by Q^4, whereas Si in the core is more associated with Q^2 or Q^1 structures.

These analyses show that in the shell region, the reaction was complete because of its dominance by Q^4 structures, where Q^2 units have been mostly removed. SEM line scans of Al and Ca across the CFA particle confirm the completion of metal-oxide bond rupture reactions in the shell region. Further, SEM line-scan results of Si across the shell show a trend of silica particles diffusing through the remaining Q^4 silica framework and dissolving into the solution at the ash/leachant interface. The concentration gradient of Si from the particle core to the core−shell boundary reflects the accumulation of silica at the boundary (i.e., the Si concentration peak in Figure 5A vi), indicating that part of the silica is trapped in the core region. The concentration gradients of Al and Ca further demonstrate that reactions in the core are incomplete. The higher abundance of Q^2 structures in the core also supports this conclusion.

The observed chemical stratification, therefore, suggests that highly crystalline ash particles develop a more silicic (Q^4-dominated) diffusion barrier region during the core-to-shell transition. This kinetically limits silica diffusion and traps a

https://doi.org/10.1021/acs.langmuir.6c02451
Langmuir 2026, 42, 23461−23470

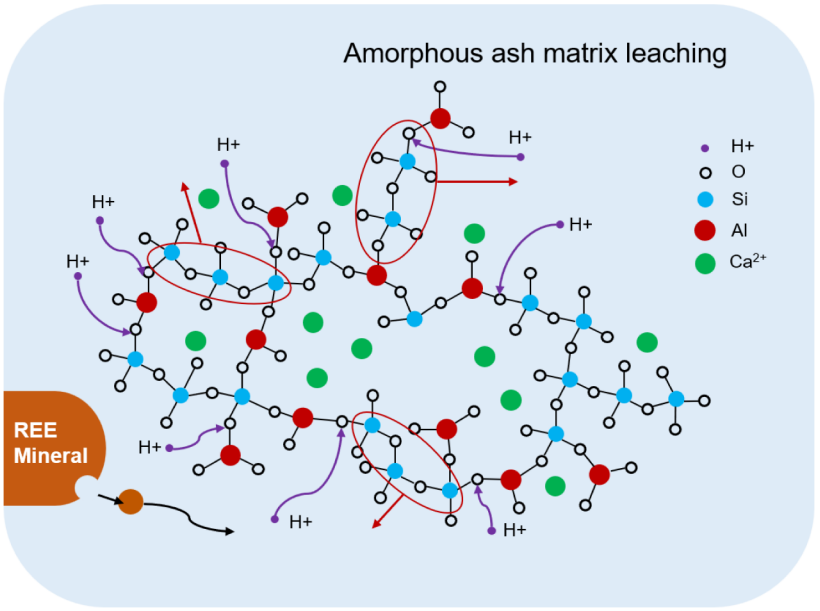

Figure 7. Acid leaching and silica gel formation mechanism model. The amorphous phase of coal fly ash, constructed primarily of −Si-O−X (X = Al, Ca), can undergo reaction with acid rapidly and release X− with silica (i.e., −Si-O− or −Si−OH). Protons attack Ca−O bonds first, followed by the bridging bonds (Si−O−Al), which break the ash framework. This creates pathways that enable exchange between matrix cations and solution protons, facilitating the release of REEs.

fraction of Si within the particle, thereby suppressing gel formation.

Silica Particle Growth Model

During the acid leaching reaction, the viscosity of the liquid phase increases in two distinct stages (Figure 6B). The first stage occurs between 10 and 15 min, where the viscosity rises from ∼1.5 cP to ∼8 cP, corresponding to the gradual formation of sols through the condensation of silica particles. The second stage takes place at ∼30 min, during which viscosity increases rapidly by ∼20-fold within 1 min. The rapid increase in leachate viscosity indicates that 30 min is the sol-to-gel transition point, consistent with the macroscopic observation of sudden gel formation and the gelation onset time. DLS measurements of dissolved particle size distributions further confirm that at ∼10 min, the dissolved silica has grown into sols (∼100 nm, Figure 6A). In the following 20 min, sol-to-gel transformation occurs with silica network reconstruction and amorphous hydrated gel formation. The increase in particle size, the change of viscosity, and the macroscopic observation of gel formation are mutually consistent and therefore provide evidence for the gelation mechanism.

Therefore, a mechanistic model for the amorphous matrix acid leaching process is described as follows (Figure 7). Acid leaching is described by two main stages: proton (H^+/H_3O^+) attack on the alkali and alkaline earth metals (i.e., Ca−O in CFA), followed by the dissolution of the bridging bonds (Si−O−Al in aluminosilicate glass). These reactions occur rapidly and remove the loosely bound silica dimers and trimers within the first 10 min of reaction.

Specifically, acid-induced Ca−O and Al−O bond rupture releases SiO_2 species and creates intraparticle pathways that facilitate solid-state interdiffusion between matrix cations and solution protons. The enhanced reagent transport subsequently promotes access to REE-bearing phases and enables their dissolution. The released silica dimers and trimers, once exiting the ash matrix, undergo hydrolysis and condensation in the leachate. The condensation of silanol groups (−Si−OH) in monosilicic acid leads to the formation of polymerized siloxane chains and ultimately three-dimensional silica gel networks.

Contrary to the common models describing silica glass corrosion under alkaline or aqueous conditions, no growth of a passivating shell encapsulating the particle was observed. Instead, gel forms throughout the leaching solution. Our analyses here show that solid-state hydrolysis of lower-energy metal-oxide bonds (e.g., Al−O) releases the cations along with non-load-bearing short-chain silica species (i.e., Q^2, Q^3) from the inert tetrameric (i.e., Q^4) silica framework. The mobilized short-chain silica then undergoes hydrolysis and condensation in the leachate solution to form polymerized siloxane networks (i.e., gels). Acid leaching does not induce a complete collapse of the particles but is more consistent with an intermediate, incomplete hydrolysis−condensation mechanism.

Our investigation on gel composition and formation shows a clear trade-off between crystallinity, gelation rates, and REE recovery rates. Specifically, to balance these competing conditions for the ash tested, we propose operating windows according to the gel formation phase diagram (Figure 2A) with an acid/ash ratio of 5:1 to 10:1 under acid concentrations of 9.5 to 10 M as the operation window for industrial processing. Additionally, given that gel formation times have been measured for different coal fly ash samples (Figure 2B: for low crystallinity samples, FA-6 at 23 min, FA-7 at 30 min, and for high crystallinity sample, FA-5 never), a quick solid−liquid separation before gel formation followed by immediate extraction could also mitigate this issue to a certain extent. The findings here present an improved gel-free approach for effective REEs extraction from CFA, with ∼90% REE recovery, producing a final leachate with 31 ppm REEs. For reference, the results here provide an ∼20% improvement over current state-of-the-art acid baking methods, where 2 h baking at 120 °C in 15 M HNO_3 solutions followed by water leaching recovered ∼74% REEs with a final REE concentration of 24 ppm in solution.[19]

https://doi.org/10.1021/acs.langmuir.6c02451
Langmuir 2026, 42, 23461−23470

CONCLUSION

This work presents a comprehensive study on the physicochemical origins of silica gelation during nitric acid leaching of coal fly ash and establishes the mechanistic link between ash crystallinity, solid-state diffusion, and leachate rheological evolution. Gels formed during acid leaching of coal fly ash are comprised of a 3D framework of Si−O bonds with Si−OH on the surface. Gel formation under highly acidic conditions proceeds through rapid proton-mediated rupture of lower-energy metal-oxide bonds (e.g., Ca−O and Al−O bonds) that liberate adjacent short-chain silica species (i.e., Q^2, Q^3), followed by diffusive transport through the glassy molecular interstices. Once in solution, the short-chain silica dimers and trimers undergo hydrolysis and condensation to form polymerized siloxane networks. Overall, gelation originates from the release and condensation of silica species derived from the amorphous phase, rather than from bulk dissolution of Si-rich particles. Amorphous-rich ashes (<10% crystallinity) exhibit rapid silica release and gelation, whereas highly crystalline ashes release insufficient silica to form gels, suppressing gelation entirely. Gel formation does not arise as a passivating layer growing on the particle surface but from incomplete hydrolysis−condensation processes occurring in the liquid phase. Accordingly, gelation does not inhibit acid attack on M−O bonds, proton exchange, or REE interdiffusion, but instead creates a secondary cage that confines REE ions after their diffusion into the liquid phase that impedes subsequent REE separation processes. For coal fly ash samples with lower crystallinity, higher REE recovery (∼80%) is achieved as the larger proportion of the amorphous phase facilitates acid-driven reactions and creates more accessible pathways for REE interdiffusion. However, these low-crystallinity samples are also more prone to gel formation, presenting a trade-off for practical REE extraction. By understanding where the gel originates and the structural and chemical factors that promote its formation, this work opens the door to avoiding gel formation during REE extraction and improving the feasibility of industrial-scale REE recovery processes, thereby simultaneously remediating and valorizing CFA as an abundant resource for rare earth elements.

ASSOCIATED CONTENT

Supporting Information

The Supporting Information is available free of charge at https://pubs.acs.org/doi/10.1021/acs.langmuir.6c02451.

Experimental details, supplemental results (Figures S1−S5), tables (Tables S1−S2), and methods (PDF)

AUTHOR INFORMATION

Corresponding Author

Wen Song − *Texas Materials Institute, The University of Texas at Austin, Austin, Texas 78712, United States; Center for Subsurface Energy and the Environment, The University of Texas at Austin, Austin, Texas 78712, United States;* orcid.org/0000-0003-1913-4503; Email: wensong@utexas.edu

Author

Yihan Li − *Texas Materials Institute, The University of Texas at Austin, Austin, Texas 78712, United States*

Complete contact information is available at: https://pubs.acs.org/10.1021/acs.langmuir.6c02451

Author Contributions

Y.L. performed all experiments, data analysis, and modeling. W.S. conceived and supervised the research. All authors discussed and contributed to writing.

Funding

This material is based upon work supported by the National Science Foundation under Grant 2145374.

Notes

The authors declare no competing financial interest.

ACKNOWLEDGMENTS

This material is based upon work supported by the National Science Foundation under Grant 2145374. The authors express gratitude to Nathaniel Miller for assistance with the ICP-MS analysis and Fu-Chun Sheu and Xun Zhan for assistance with TEM imaging.

REFERENCES

(1) Gupta, G. K.; Krishnamurthy, N. Extractive Metallurgy of Rare Earths. *Int. Mater. Rev* **1992**, *37* (1), 197−248.

(2) Pulido-Sánchez, D.; Capellán-Pérez, I.; de Castro, C.; Frechoso, F. Material and Energy Requirements of Transport Electrification. *Energy Environ. Sci* **2022**, *15* (12), 4872−4910.

(3) Zhang, S.; Zeng, Z.; Li, Q.; Huang, B.; Zhang, X.; Du, Y.; Yan, C. H. Lanthanide Electronic Perturbation in Pt-Ln (La, Ce, Pr and Nd) Alloys for Enhanced Methanol Oxidation Reaction Activity. *Energy Environ. Sci* **2021**, *14* (11), 5911−5918.

(4) IEA*Global Critical Minerals Outlook 2024*IEA2024282

(5) Yin, X.; Martineau, C.; Demers, I.; Basiliko, N.; Fenton, N. J. The Potential Environmental Risks Associated with the Development of Rare Earth Element Production in Canada. *Environ. Rev* **2021**, *29* (3), 354−377.

(6) Zapp, P.; Schreiber, A.; Marx, J.; Kuckshinrichs, W. Environmental Impacts of Rare Earth Production. *MRS Bull* **2022**, *47* (3), 267−275.

(7) Dutta, T.; Kim, K. H.; Uchimiya, M.; Kwon, E. E.; Jeon, B. H.; Deep, A.; Yun, S. T. Global Demand for Rare Earth Resources and Strategies for Green Mining. *Environ. Res* **2016**, *150*, 182−190.

(8) Gür, T. M. Review of Electrical Energy Storage Technologies, Materials and Systems: Challenges and Prospects for Large-Scale Grid Storage. *Energy Environ. Sci* **2018**, *11* (10), 2696−2767.

(9) Ketris, M. P.; Yudovich, Y. E. Estimations of Clarkes for Carbonaceous Biolithes: World Averages for Trace Element Contents in Black Shales and Coals. *Int. J. Coal Geol* **2009**, *78* (2), 135−148.

(10) Franus, W.; Wiatros-Motyka, M. M.; Wdowin, M. Coal Fly Ash as a Resource for Rare Earth Elements. *Environ. Sci. Pollut. Res* **2015**, *22* (12), 9464−9474.

(11) Taggart, R. K.; Hower, J. C.; Dwyer, G. S.; Hsu-Kim, H. Trends in the Rare Earth Element Content of U.S.-Based Coal Combustion Fly Ashes. *Environ. Sci. Technol* **2016**, *50* (11), 5919−5926.

(12) American Road & Transportation Builders Association (ARTBA) 2024. *Mid-Year Update to the Annual U.S. Transportation Construction Forecast*. American Road & Transportation Builders Association (ARTBA) 2024 2024.

(13) Yao, Z. T.; Ji, X. S.; Sarker, P. K.; Tang, J. H.; Ge, L. Q.; Xia, M. S.; Xi, Y. Q. A Comprehensive Review on the Applications of Coal Fly Ash. *Earth-Sci. Rev* **2015**, *141*, 105−121.

(14) Shaheen, S. M.; Hooda, P. S.; Tsadilas, C. D. Opportunities and Challenges in the Use of Coal Fly Ash for Soil Improvements - A Review. *J. Environ. Manage* **2014**, *145*, 249−267.

(15) Sahoo, P. K.; Kim, K.; Powell, M. A.; Equeenuddin, S. M. Recovery of Metals and Other Beneficial Products from Coal Fly Ash: A Sustainable Approach for Fly Ash Management. *Int. J. Coal Sci. Technol* **2016**, *3* (3), 267−283.

(16) Bian, Z.; Dong, J.; Lei, S.; Leng, H.; Mu, S.; Wang, H. The Impact of Disposal and Treatment of Coal Mining Wastes on Environment and Farmland. *Environ. Geol* **2009**, *58* (3), 625−634.
(17) Gerardo, S.; Davletshin, A. R.; Loewy, S. L.; Song, W. From Ashes to Riches: Microscale Phenomena Controlling Rare Earths Recovery from Coal Fly Ash. *Environ. Sci. Technol* **2022**, *56* (22), 16200−16208.
(18) Gerardo, S.; Matthews, K.; Warner, J.; Song, W. Role of Nanoscale Crystallinity on the Recovery of Rare Earth Elements (REEs) from Coal Fly Ash. *Environ. Sci. Technol. Lett* **2023**, *10* (10), 943−948.
(19) Gerardo, S.; Song, W. Rare Earths Recovery from Calcium-Rich Coal Fly Ash: Secondary Phase Formation and Mitigation Approaches. *Environ. Sci. Technol* **2025**, *59*, 23592.
(20) Battsengel, A.; Batnasan, A.; Narankhuu, A.; Haga, K.; Watanabe, Y.; Shibayama, A. Recovery of Light and Heavy Rare Earth Elements from Apatite Ore Using Sulphuric Acid Leaching, Solvent Extraction and Precipitation. *Hydrometallurgy* **2018**, *179* (May), 100−109.
(21) Gin, S.; Neill, L.; Fournier, M.; Frugier, P.; Ducasse, T.; Tribet, M.; Abdelouas, A.; Parruzot, B.; Neeway, J.; Wall, N. The Controversial Role of Inter-Diffusion in Glass Alteration. *Chem. Geol* **2016**, *440*, 115−123.
(22) Cailleteau, C.; Angeli, F.; Devreux, F.; Gin, S.; Jestin, J.; Jollivet, P.; Spalla, O. Insight into Silicate-Glass Corrosion Mechanisms. *Nat. Mater* **2008**, *7* (12), 978−983.
(23) Hellmann, R.; Cotte, S.; Cadel, E.; Malladi, S.; Karlsson, L. S.; Lozano-Perez, S.; Cabié, M.; Seyeux, A. Nanometre-Scale Evidence for Interfacial Dissolution-Reprecipitation Control of Silicate Glass Corrosion. *Nat. Mater* **2015**, *14* (3), 307−311.
(24) Thomas, B. S.; Dimitriadis, P.; Kundu, C.; Vuppaladadiyam, S. S. V.; Raman, R. K. S.; Bhattacharya, S. Extraction and Separation of Rare Earth Elements from Coal and Coal Fly Ash: A Review on Fundamental Understanding and on-Going Engineering Advancements. *J. Environ. Chem. Eng* **2024**, *12* (3), 112769.
(25) Saha, D.; Clarke, J. S.; Altman, S. H.; McCann, M. A.; Kamara, R. S.; Gordy, A.; Kervick, T. Selective Extraction and Recovery of Rare Earth Elements from Coal Fly Ash by Carboxylated Mesoporous Carbon. *Sep. Purif. Technol* **2025**, *354* (P5), 129153.
(26) Deshmane, V. G.; Islam, S. Z.; Bhave, R. R. Selective Recovery of Rare Earth Elements from a Wide Range of E-Waste and Process Scalability of Membrane Solvent Extraction. *Environ. Sci. Technol* **2020**, *54* (1), 550−558.
(27) Lv, Z.; Zhang, X.; Gao, Q.; Wen, C.; He, Y.; Tan, H.; Qian, L.; Qi, W.; Chen, X.; Li, Z. Synergistic Nanoarchitectonics: Precision Membrane Engineering for Rare Earth Selective Separation. *Adv. Funct. Mater* **2024**, *34* (36), 2409274.
(28) Moldoveanu, G. A.; Papangelakis, V. G. An Overview of Rare-Earth Recovery by Ion-Exchange Leaching from Ion-Adsorption Clays of Various Origins. *Mineral Mag* **2016**, *80* (1), 63−76.
(29) Cho, E.; Jung, Y.; Choi, J. W.; Lee, C.; Jung, K. W. Hybrid Strategy for In Situ Shaping of Zeolite-Imidazolate-Frameworks into Polymeric Macrocapsule: Toward Practical Applications of Rare Earth Element Recovery. *Adv. Funct. Mater* **2024**, *34* (49), 1−13.
(30) Izquierdo, M.; Querol, X. Leaching Behaviour of Elements from Coal Combustion Fly Ash: An Overview. *Int. J. Coal Geol* **2012**, *94*, 54−66.
(31) Hoyos-Montilla, A. A.; Tobón, J. I.; Puertas, F. Role of Calcium Hydroxide in the Alkaline Activation of Coal Fly Ash. *Cem. Concr. Compos* **2023**, *137*, 104925.
(32) Liu, B.; Yue, B.; He, L. L.; Meng, B. B.; Wang, Y. X.; Wang, T.; Gao, H. Synergistic Solidification and Mechanism Research of Electrolytic Manganese Residue and Coal Fly Ash Based on C-A-S-H Gel Material. *J. Environ. Manage* **2024**, *365*, 121600.
(33) Jennings, H. M. Aqueous Solubility Relationships for Lhvo Types of Calcium Silicate Hydrate. *J. Am. Ceram. Soc* **1986**, *69* (8), 614−618.
(34) Iler, R. K. *The Chemistry of Silica: Solubility, Polymerization, Colloid and Surface Properties, and Biochemistry*. Wiley 1979.
(35) Gin, S.; Collin, M.; Jollivet, P.; Fournier, M.; Minet, Y.; Dupuy, L.; Mahadevan, T.; Kerisit, S.; Du, J. Dynamics of Self-Reorganization Explains Passivation of Silicate Glasses. *Nat. Commun* **2018**, *9* (1), 1−9.
(36) Dove, P. M.; Han, N.; Wallace, A. F.; De Yoreo, J. J. Kinetics of Amorphous Silica Dissolution and the Paradox of the Silica Polymorphs. *Proc. Natl. Acad. Sci. U. S. A* **2008**, *105* (29), 9903−9908.
(37) Neeway, J. J.; Kerisit, S. N.; Liu, J.; Zhang, J.; Zhu, Z.; Riley, B. J.; Ryan, J. V. Ion-Exchange Interdiffusion Model with Potential Application to Long-Term Nuclear Waste Glass Performance. *J. Phys. Chem. C* **2016**, *120* (17), 9374−9384.
(38) Kunhi Mohamed, A.; Moutzouri, P.; Berruyer, P.; Walder, B. J.; Siramanont, J.; Harris, M.; Negroni, M.; Galmarini, S. C.; Parker, S. C.; Scrivener, K. L.; et al. The Atomic-Level Structure of Cementitious Calcium Aluminate Silicate Hydrate. *J. Am. Chem. Soc* **2020**, *142* (25), 11060−11071.
(39) Hopf, J.; Eskelsen, J. R.; Chiu, M.; Ievlev, A. V.; Ovchinnikova, O. S.; Leonard, D.; Pierce, E. M. Toward an Understanding of Surface Layer Formation, Growth, and Transformation at the Glass−Fluid Interface. *Geochim. Cosmochim. Acta* **2018**, *229*, 65−84.
(40) Gin, S.; Mir, A. H.; Jan, A.; Delaye, J. M.; Chauvet, E.; De Puydt, Y.; Gourgiotis, A.; Kerisit, S. A General Mechanism for Gel Layer Formation on Borosilicate Glass under Aqueous Corrosion. *J. Phys. Chem. C* **2020**, *124* (9), 5132−5144.
(41) *Specification for Coal Fly Ash and Raw or Calcined Natural Pozzolan for Use in Concrete*. ASTM International: West Conshohocken, PA, 2012. .
(42) Redlich, O.; Duerst, R. W.; Merbach, A. Ionization of Strong Electrolytes. XI. The Molecular States of Nitric Acid and Perchloric Acid. *J. Chem. Phys* **1968**, *49* (7), 2986−2994.
(43) Levanov, A. V.; Isaikina, O. Y.; Lunin, V. V. Dissociation Constant of Nitric Acid. *Russ. J. Phys. Chem. A* **2017**, *91* (7), 1221−1228.
(44) Irish, D. E.; Puzic, O. Raman Spectral Study of the Constitution and Equilibria of Nitric Acid and D-Nitric Acid. *J. Solution Chem* **1981**, *10* (6), 377−393.
(45) Zagrajczuk, B.; Dziadek, M.; Olejniczak, Z.; Sulikowski, B.; Cholewa-Kowalska, K.; Laczka, M. Structural Investigation of Gel-Derived Materials from the SiO2−Al2O3 System. *J. Mol. Struct* **2018**, *1167*, 23−32.
(46) Garvie, L. A. J.; Buseck, P. R. Bonding in Silicates: Investigation of the Si L 2,3 Edge by Parallel Electron Energy-Loss Spectroscopy. *Am. Mineral.* **1999**, *84*, 946−964.
(47) Zhang, N.; Huang, H. D.; Yang, R.; Zheng, A.; Moment, A. Aqueous Metal Ion Leaching Processes from High Sulfur Coal Fly Ash for Carbon Mineralization: The Importance of PH Control on Cation Extraction, Carbonate Purity, and Silicon Q Structure. *Chem. Eng. J* **2023**, *474*, 145968.

https://doi.org/10.1021/acs.langmuir.6c02451
Langmuir 2026, 42, 23461−23470